RESEARCH ARTICLE

ADVANCED OPTICAL MATERIALS
www.advopticalmat.de

2D-Material-Fused High-Emittance Plasmo–Photonic Metasurfaces

Masanobu Iwanaga, Xu Yang, Vasilios Karanikolas, Takashi Kuroda, and Yoshiki Sakuma*

Transition metal dichalcogenides (TMDC) are a family of atomic-layer 2D materials (2dMs). Many researches have attempted to reinforce the unique properties by incorporating artificially designed nanostructures. Here, a highly photoluminescence (PL) enhancing platform is reported that is formed by combining high-emittance plasmo–photonic metasurfaces with a large-area 2dM, which is a continuous monolayer of TMDC of cm^2 dimension. It is experimentally demonstrated that the 2dM-PL intensity at room temperature is enhanced by more than 1030-fold in comparison with that observed on the flat gold film regions. The enhancement is associated with spectral transformation indicating a resonant effect of the metasurfaces. It is moreover revealed that the confocal PL image originates from a coherent single-mode emission that forms a photon number distribution obeying the Poisson probability distribution. Thus, the 2dM-fused metasurfaces function as efficient coherent quantum light sources. PL decay-time analysis also reveals the coexistence of two components in the enhanced PL. The fast component exhibits a lifetime of 18 ps whereas the slow component decays at 4.4 ns. Both components are most likely to undergo radiative processes, which indicates that metal-induced PL quenching is suppressed on these 2dM-fused metasurfaces. The long lifetime component is ascribed to an excitonic intervalley transition.

1. Introduction

Quantum 2D materials (2dM) such as transition metal dichalcogenides (TMDCs) are attracting great interest as a new series of atomic-layer materials that exhibit remarkable optical[1–3] and electronic[4,5] properties owing to the peculiar band structures originating from the ultimately thin 2D structures. Numerous studies have been conducted to clarify the basic properties of the TMDC atomic layers. For future applications, large-scale growth is also being studied to enable the production of wafer-scale TMDC monolayers.[6–9]

By combining the direct-bandgap luminescence of TMDC monolayers with surface-enhancing effects that are attempted to be artificially realized on metasurfaces and nanostructures, novel and highly efficient light-emitting systems showing spontaneous emissions[10–27] and a stimulated emission[28] have been extensively explored. The stimulated emission was reported using a photonic crystal cavity whereas the contrast of the stimulated emission to spontaneous emission was not so high, being ≈10;[28] it is thus unclear whether the stimulated emission deserves practical use. Let us hereafter focus on spontaneous emissions from TMDC monolayers. To date, most trials have reported a few tenfold spontaneously photoluminescence (PL) intensity enhancement. This tendency suggests that the interplay between the TMDC monolayer and the artificial nanostructures was insufficient in the most cases, where local electric-field enhancement (or so-called hot spot) was thought highly of at either of excitation or emission wavelength. To our knowledge, the largest PL-intensity enhancement factor (EF) using plasmonic platforms was approximately 200-fold regarding the WSe_2 monolayer transferred on Au nanogap structures under excitation at 532 nm[15] and MoS_2 monolayer placed between Ag nanocube and Au film under excitation at 420 nm.[18] We point out that artificial manipulations for PL-intensity EF were conventionally conducted by dividing the observed EFs with geometrical factors, which were typically ratio of nanogap width to diameter of excitation laser spot and took small values in a range from 1/100 to 1/10; consequently, far larger PL-intensity EFs than the observed EFs were claimed in the previous reports;[10,12,15,18,19] however, these artificially manipulated EFs are not observable and are practically meaningless because the geometrical factors mix up the observed quantity with effects under the diffraction limit.

Apart from the artificially manipulated EFs, optical resonances in the artificial nanostructures were expected to selectively enhance the exciton transitions in the TMDC monolayer. However,

M. Iwanaga, X. Yang[+], V. Karanikolas[++], T. Kuroda, Y. Sakuma
National Institute for Materials Science (NIMS)
1-1 Namiki, Tsukuba 305-0044, Japan
E-mail: iwanaga.masanobu@nims.go.jp

The ORCID identification number(s) for the author(s) of this article can be found under https://doi.org/10.1002/adom.202303309

[+]Present address: Institute of Materials and Systems for Sustainability, Nagoya University, Nagoya 464-8601, Japan

[++]Present address: Materials Modelling, Institute of Materials Science, Technical University of Darmstadt, 64287 Darmstadt, Germany

DOI: 10.1002/adom.202303309

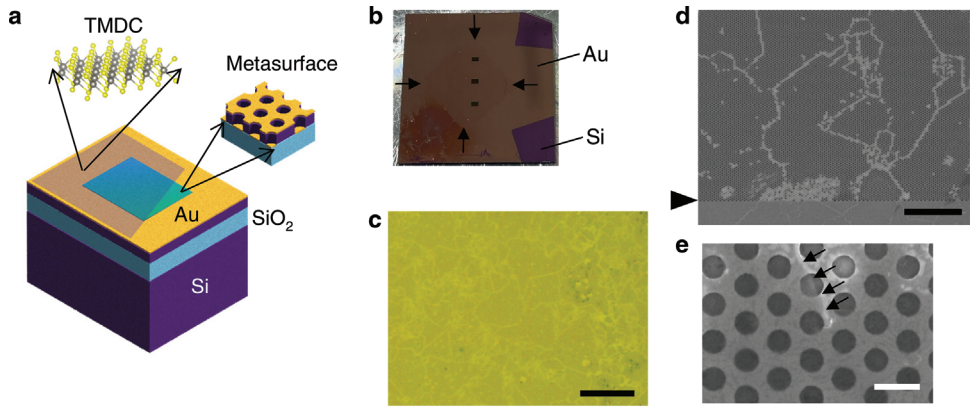

Figure 1. Structural overview. a) Illustration of a 2D material (2dM) transferred onto a plasmo–photonic metasurface. b) Photo of a 2dM-fused metasurface substrate. Three metasurfaces are located vertically at the center of the substrate. Four arrows indicate the corners of the 2dM monolayer. c) Optical microscopy image with black scale bar of 50 μm. d) Top-view scanning-electron-microscopy (SEM) image, taken near the edge of metasurface. The triangle indicates the edge. 2dM-fused flat Au region is located near the lower edge. The black scale bar indicates 10 μm. e) Magnified SEM image. Arrows indicate the edges of the 2dM film. The white scale bar indicates 500 nm.

the resonances did not contribute to significant changes in the TMDC PL spectra, except for a plasmon-based study incorporating MoS_2[18] and dielectric nanophotonic structures coupled with WSe_2;[25] in the former,[18] sub-10 nm gap between Ag nanocube and Au file was used for the enhanced PL experiment, the PL EF for *A* exciton was 17-fold and that for *B* exciton was 211-fold, and the *B* exciton was particularly enhanced under excitation wavelength at 420 nm, which was matched with a wavelength of nanogap cavity resonance; in the latter,[25] the PL was measured only at 5 K to study single-photon emissions, the temperature dependence of the PL spectra was not examined, and consequently resonant effect for the spectral shapes coming from the dielectric nanostructures is difficult to be evaluated here.

As another drawback in the previous studies, the TMDC monolayers were limited to micro-domains, which were typically triangles of several-micrometer sides and resulted in small light-emitting devices for most practical use. It is highly preferred that monolayers of larger scale are used for the light-emitting devices.

A plasmo–photonic metasurfaces have eigen modes at 600–1400 nm, resulting from coupling of plasmonic and photonic guided modes, and exhibit a feature that they have several large light absorption bands.[29] Absorptance is equivalent to emittance due to reciprocity.[30] Emittance is a macroscopic property of metasurfaces and does not depend on local hot spots. The metasurfaces exhibited extremely efficient fluorescence (FL) enhancing capabilities that exceed 2000-fold.[31,32] In particular, the metasurfaces coated with a self-assembled monolayer suppressed metal-induced FL quenching[31] and selectively enhanced Raman scattering with controlling the interface between the molecules and the metasurfaces.[32] Recently, the metasurfaces have been shown to serve as high-precision FL biosensors.[33] All-dielectric metasurfaces consisting of periodic Si-nanopellet arrays exhibited a similar capability of enhancing FL[34,35] and have been applied to biosensing.[36–41] These two types of metasurfaces have opened new routes for developing extremely efficient biosensors.

Here, we report a new platform fusing a continuous TMDC monolayer with the plasmo–photonic metasurfaces, which have the macroscopic feature of high emittance and do not rely on the conventional hot-spot strategy. To date, the plasmo–photonic metasurface have not been applied to any platform including 2dM. Optical properties and resonances of the metasurface are numerically clarified. Strong PL enhancement is presented on the resonance and the enhanced PL dynamics is examined by analyzing PL decay time. Furthermore, a coherent single-mode emission including single-photon emissions is revealed through analysis for photon number distributions of confocal PL images. Additionally, Raman-scattering enhancement is addressed.

2. Results and Discussion

2.1. 2dM-Fused Metasurfaces

Figure 1a schematically illustrates a plasmo–photonic metasurface fused with a TMDC monolayer, which was visualized using VESTA software.[42] The monolayer was nearly WS_2, described in the Experimental Section; the gray and yellow spheres denote W and S atoms, respectively. The monolayer was transferred onto a metasurface substate conducting a procedure described in the Experimental Section.

The appearance of the 2dM-fused metasurface substrate is shown in Figure 1b. The metasurface substrate was approximately a square of 2 cm × 2 cm, based on a silicon-on-insulator (SOI) substrate (top Si layer 200 nm/middle buried oxide 375 nm/base Si wafer 675 μm). The TMDC atomic layer with an area of approximately 1 cm^2, whose corners are indicated by arrows, was transferred onto three metasurface areas of 0.96 mm × 0.60 mm, which were fabricated along the vertical center line of the substrate. The nanofabrication procedures of the metasurfaces are described in the Experimental Section.

An optical microscopy image of the TMDC-transferred metasurface is shown in Figure 1c, where the black scale bar indicates 50 μm. The optical image indicates that the transferred TMDC film was sectioned on the metasurface by forming boundaries, mainly resulting from wrinkles and rifts that emerged during the transfer process. Magnified images were obtained using field-emission scanning electron microscopy (SEM), as shown in Figure 1d,e, with black and white scale bars of 10 μm and 500 nm, respectively. The triangle in Figure 1d indicates the border

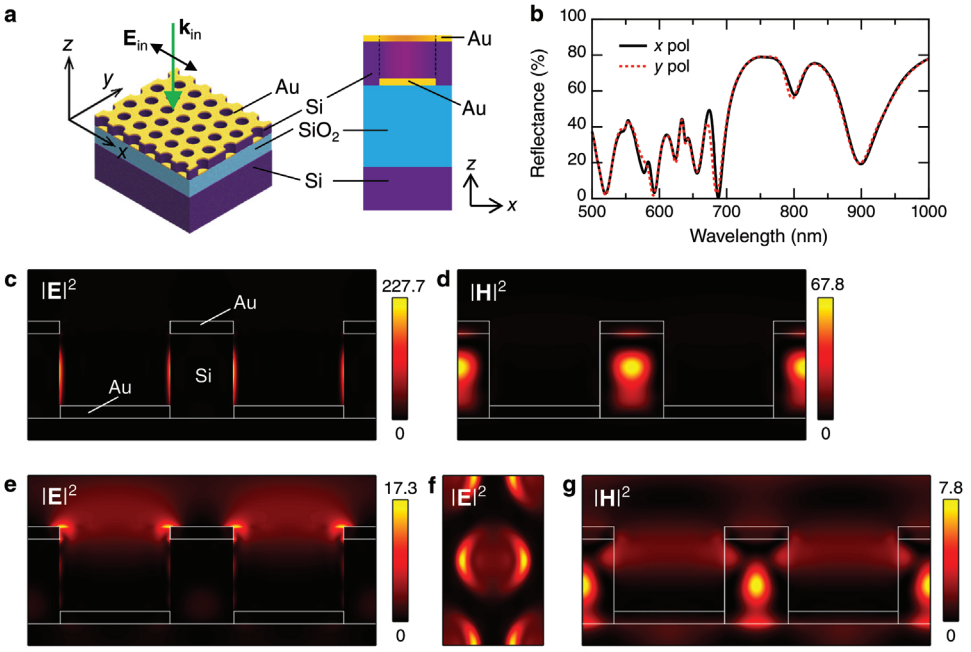

Figure 2. Optical resonances of the plasmo–photonic metasurface. a) Optical configuration and *xyz* coordinate: 3D view (left) and *xz*-section view (right). b) Simulated reflectance spectra at *x* and *y* polarizations, shown with black solid and red dotted lines, respectively. c,d) Resonant electric- and magnetic-field intensity distributions at 638.9 nm in an *xz*-section view, respectively. e,f) Electric-field intensity distributions at 532.0 nm in *xz*- and *xy*-section views, respectively. g) Magnetic-field intensity distribution at 532.0 nm in the *xz*-section view that is the same with (e). We note that incident intensity was set to unity in common to (c–g).

between the metasurface area (upper) and flat Au region (lower). The boundaries and flat-less regions in the TMDC layer are observed as white parts. Other regions are flat. The TMDC layer is mostly flat in the Au region. In the magnified SEM image in Figure 1e, a rift of the TMDC layer is indicated by arrows and seen as a white part because the outermost surface is Au, which is brighter than that of the TMDC layer. Figure 1e also shows that the TMDC layer except for the rifts covers the metasurface, including the air holes.

2.2. Electromagnetic Resonances of Metasurface

Figure 2 shows the reflectance spectra and the resonant electromagnetic (EM) field distributions of the plasmo–photonic metasurface. The optical configuration and *xyz* coordinates are illustrated in Figure 2a:3D (left) and a *xz*-section views (right), respectively. The metasurface includes a periodic hexagonal array of air holes; the periodic length was set to 410 nm and the diameter of the hole 260 nm, indicated by dotted lines in the *xz* section. Thickness of Au and Si layers was 30 and 200 nm, respectively. Incident wavevector $\mathbf{k}_{in}$ and polarization $\mathbf{E}_{in}$ are shown in the 3D view.

The computed reflectance spectra at the normal incidence are shown in Figure 2b. The incident polarization ($\mathbf{E}_{in}$) was set to *x*- or *y*-polarization, as shown with solid black and dotted red curves, respectively. More than ten resonances appear in the reflectance spectra as peaks and dips. The dependence on the incident polarizations is not significant at the normal incidence.

A set of resonant EM-field intensity distributions at 638.9 nm, which corresponds to a dip in the reflectance spectra, is shown in Figure 2c,d, where an *xz*-section view through the center of the circular air holes is presented. The electric-field intensity is dominantly localized and significantly enhanced at the sidewall of the Si nanohole, reaching at the maximum of 227.7 when the incident electric-field intensity is set to 1.0. Accordingly, the magnetic-field intensity is the most enhanced, inside the Si layer between the strong electric fields, at the maximum intensity of 67.8. Both EM components are significantly enhanced in the metasurface compared with the incidence. Simultaneously, the EM fields are strongly localized in the metasurface, implying that the transmission component is small. This point is quantitatively addressed later (**Figure 3**).

At the excitation wavelength of 532.0 nm for the PL spectra, the electric-field intensity distribution is the most enhanced at the top of Au layer, as shown in Figure 2e, where the *xz* section through the center of the air holes is presented. Figure 2f shows an *xy* section representing the unit cell of the metasurface and locating 0.5 nm above the top of the perforated Au layer. The *xy* section corresponds to the position of the transferred TMDC monolayer. The maximum of the electric-field intensity is 17.3, which is enhanced but not as strong as that at 638.9nm (Figure 2c). The magnetic field in the *xz*-section is shown in Figure 2g in a similar manner to Figure 2e, and is the most enhanced in the Si layer, though the field intensity is substantially weaker than that at 638.9 nm.

To explicitly evaluate the emittance of the plasmo–photonic metasurface, we studied the metasurface on a transparent SiO_2 substrate, as illustrated in Figure 3a. The experimental SOI configuration in Figure 2a includes light absorption by the base Si substrate. Consequently, it is difficult to identify light absorption by the metasurface alone.

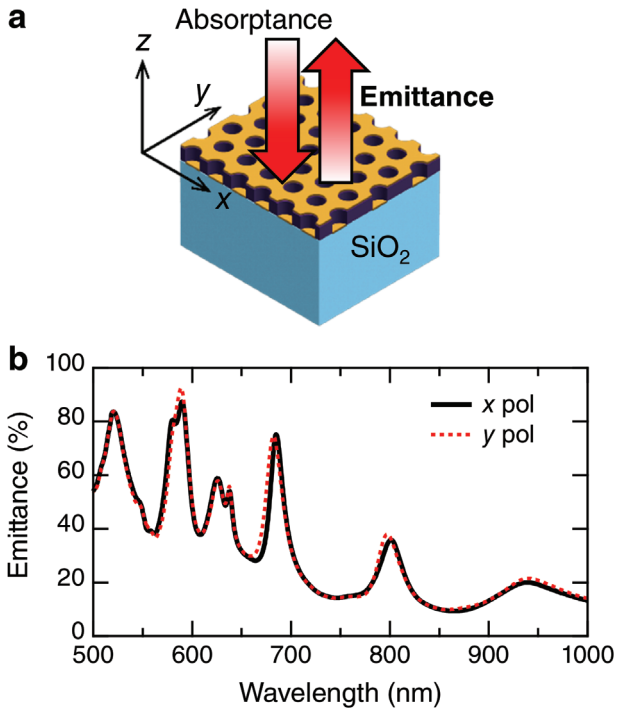

Figure 3. Emittance of plasmo–photonic metasurface. a) 3D-view illustration of the metasurface on SiO_2 substrate. Directions of light absorptance and emittance are indicated by arrows. b) Computed emittance spectra at *x* and *y* polarizations, evaluated by using Equation (1) and shown with solid black and dotted red curves, respectively.

The emittance is equivalent to the absorptance because of reciprocity,[30] therefore, the two quantities are equal. Both quantities are macroscopic parameters of the metasurface. We evaluated the absorptance (*Abs*) in % using Equation (1):

$$Abs = 100 - \sum_{m,n}(R_{m,n} + T_{m,n}) \tag{1}$$

where m and n denote the diffraction orders open in the wavelength range of interest. $R_{0,0}$ and $T_{0,0}$ are the ordinary reflectance and transmittance, respectively. The nonzero diffraction orders were $R_{0,\pm1}$, $T_{\pm1,0}$, $T_{0,\pm1}$, $T_{0,\pm2}$, and $T_{\pm1,\pm1}$ in the present wavelength range. Figure 3b shows polarization-dependent *Abs* spectra (*x* polarization:solid black curve, *y* polarization:dotted red curve) and several prominent emittance peaks, some of which exceed 80%. The emittance peaks originate from the resonances of the plasmo–photonic metasurface because the other surrounding materials, namely air and SiO_2, are resonance-free in this wavelength range. Figure 3b also shows that 56% of the incident light at 532 nm is resonantly absorbed; in other words, the emittance is 56% at this wavelength. The emittance peak overlaps with the PL wavelengths of the TMDC monolayer, as shown later. The resonant electric fields are significantly enhanced, as visualized in Figure 2c,e,f.

2.3. Photoluminescence Enhancement in the 2dM-Fused System

The enhanced PL (red curve) and the reference spectra measured on flat Au (thin yellow lines) are shown in **Figure** 4a, and the inset magnifies the reference PL spectrum. The PL EF is plotted for the right axis with a dotted black curve where the EF was defined as the ratio of the enhanced PL and reference spectra. The maximum PL EF was 1033-fold and located at 634.2 nm. Thus, prominent PL enhancement was quantitatively evaluated. The enhanced PL peaks at 636.7 and 670 nm are ascribed to the *A* exciton and trion, respectively, in the TMDC monolayer.[43] A small peak at 563 nm is considered to originate from the *B* exciton. The largest PL peak at 636.7 nm agrees with a measured reflectance dip (or an emittance peak) of the 2dM-fused metasurface, as shown in the Supporting Information (Figure S1, Supporting Information). Thus, the prominent PL enhancement is a resonant effect incorporating the metasurface.

The PL peak of the reference spectrum was 644 nm and differed from the peak of the enhanced PL at 636.7 nm. The PL spectra of the TMDC monolayers have been reported frequently. It is known that the spectra can change due to circumstances, including the substrate,[43–47] atomic components,[48,49] and oxidation.[50] In this case, the as-grown TMDC layer was transferred onto the metasurface using an organic sorbent; therefore, the chemical treatment and the change of substrate were considered to change the PL peak to some extent. However, as we noted above, the most PL-enhanced wavelength agrees with the resonant wavelength of this 2dM-fused system and therefore is primarily ascribed to the resonant effect of metasurface. Besides, oxidation could explicitly change the PL peak after exposure to air for more than 7 d;[50] however, we handled the TMDC sample in air within 12 h or less, and preserved it under an N_2 gas atmosphere except for experiment; therefore, the oxidation is unlikely in this case. We briefly note that the PL-peak wavelength is within the range reported so far.[44,48,49]

The PL EF in the experimental configuration is expressed as[31,51]

$$\mathrm{EF} = \frac{N_m}{N_0} \times \frac{\eta_m}{\eta_0} \times \frac{\gamma_m(\mathbf{k})}{\gamma_0(\mathbf{k})} \tag{2}$$

where the subscripts m and 0 denote on and off the metasurface, respectively. N is the photoexcited populations, η is the quantum yield, and $\gamma(\mathbf{k})$ is the radiative decay rate dependent on outgoing wavevector $\mathbf{k}$. In particular, $\eta = \gamma/(\gamma + \gamma_{NR})$ where γ_{NR} is the nonradiative decay rate. The γ_m/γ_0 ratio is often referred to as the Purcell factor.[52] From the electric-field intensity in Figure 2e, the TMDC monolayer was excited efficiently by ≈tenfold, giving the N_m/N_0 ratio. The other factors at the right-hand side of Equation (2) are considered after examining the experimental and theoretical results.

An upright confocal PL image of the 2dM-fused metasurface is shown in Figure 4b. Red denotes the PL from the 2dM monolayer. The rectangular red area corresponds to the metasurface area of 0.96 mm × 0.60 mm. The white scale bar indicates 0.25 mm. The off-metasurface area is dark, exhibiting the zero-signal level in the confocal measurement. We also mention that the brightest spot on the bottom edge of the metasurface originated from the aggregated 2dM that was not a simple monolayer. The confocal image was acquired through the photon-counting measurement (see the Experimental Section for details). Each pixel has a detected photon number. Therefore, the photon number distribution can be extracted as shown in Figure 4c. The

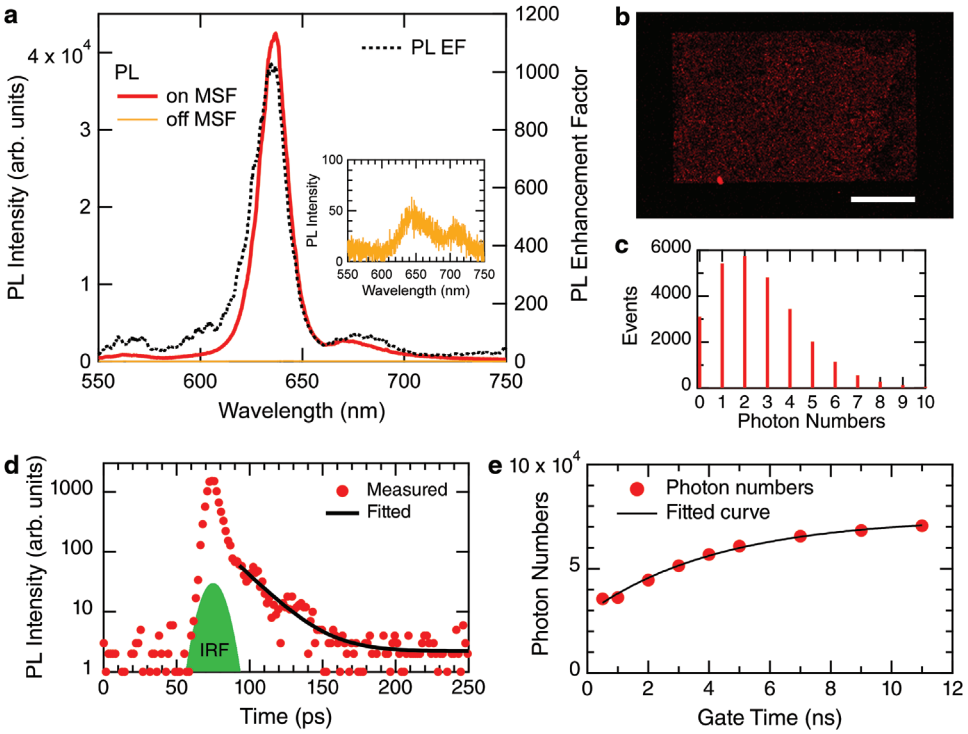

Figure 4. Enhanced photoluminescence (PL) from the 2dM-fused metasurface (MSF). a) PL spectra on and off the MSF, shown with a solid red curve and thin yellow lines, respectively. Inset shows a magnified PL spectrum off the MSF. The PL enhancement factor (EF) is represented with a dotted black curve, plotted for the right axis. b) Confocal PL image represented using a pseudo red color. Rectangular red area at the center corresponds to the MSF. White scale bar indicates 250 μm. c) Photon number distribution evaluated in the confocal image in (b). d,e) Temporal profiles of the enhanced PL in ps and ns ranges, respectively. Measured data are shown with closed red circles. Fitted exponential curves are shown with black curves.

analysis region for the photon numbers was set inside the metasurface area by choosing a nearly uniform area, which is shown in the Supporting Information (Figure S2, Supporting Information). Figure 4c shows that the photon numbers were predominantly less than ten in each pixel and that single-photon detection from the TMDC monolayer occupied 20.3% of the photon number distribution. Conducting fitting using the Poisson distribution, we reproduced the photon number distribution fairly well (Figure S3, Supporting Information) and determined the mean photon number to be 2.41 for Figure 4c. The zero-photon events occupying 11.6% are primarily attributable to the Poisson distribution that governs the probability of small-number events. Small deviation from the ideal Poisson distribution probably resulted from broken holes in the monolayer and a small portion of bilayers. Overall, the photon number distribution obeying the Poisson distribution is ascribed to a coherent single-mode photon emission;[53] in other words, this 2dM-fused system is a quantum coherent light source.

We note that, as a corollary of the coherent single-mode emission obeying the Poisson distribution, the second-order coherence $g^{(2)}$ is unity, meaning perfect coherence, irrespective of the mean photon number;[53] in other word, the photon number distribution obeying the Poisson distribution is direct evidence for the quantum coherent state. To the best of our knowledge, the coherent state has not been observed on any plasmonic platform. Regarding the appearance of Figure 4b, we note that dark spots exist on the metasurface area and result from the quantum nature of light emission, which means that the zero-photon spots appear inevitably under low-power excitation.

The PL decay profile in a ps range is shown on the semi-log scale in Figure 4d; closed red circles denote the measured PL data and the solid black curve is a fitted curve using a single-exponential function such as $y = y_0 + A_0 \exp[-(t - t_0)/\tau_S]$ where τ_S denotes the decay time, A_0 is the proportional constant, t_0 is the time offset, and y_0 is the background constant. The measured data were fitted 15 ps after from the peak because the temporal width of the excitation laser pulses was determined by the instrumental response function (IRF) in the setup and was approximately 10 ps at the full width at half maximum.[54] The IRF is shown in green in Figure 4d. Thus, the PL decay time in the ps range was determined to be $\tau_S = 18.0 \pm 1.2$ ps.

The PL lifetime was also studied in a ns range. The temporal PL growth is shown with red dots in Figure 4e, where the photon numbers were accumulated using a photon-counting detector. The time-integrated PL intensity I for the gate time T is expressed as

$$I(T) = \int_0^T [C\exp(-t/\tau_S) + D\exp(-t/\tau_L)]dt \approx C\tau_S + D\tau_L[1 - \exp(-T/\tau_L)] \quad (3)$$

where τ_S and τ_L denote the short and long decay times, respectively, and C and D are the proportional constants. A relation of

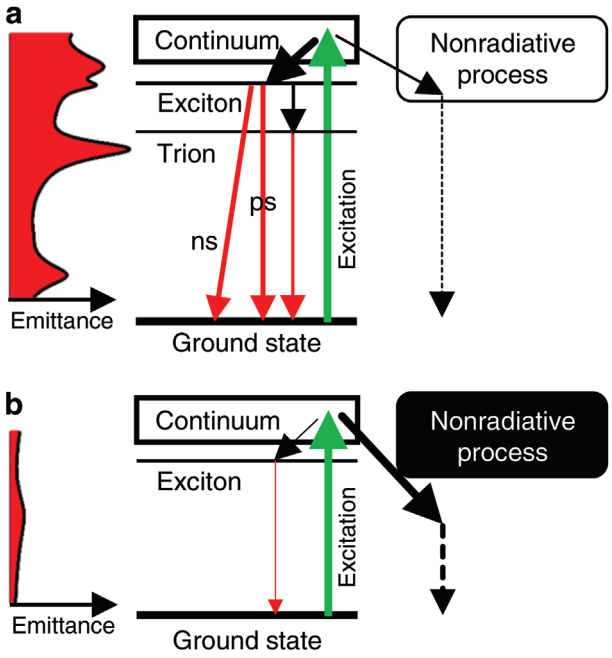

Figure 5. Energy diagrams of the PL dynamics. a) Enhanced PL processes on the plasmo–photonic metasurface. b) Excitation–relaxation dynamics off the metasurface (i.e., on the flat Au film), where the nonradiative process(es) is predominant.

$\tau_S \ll T$ is reasonably assumed to derive Equation (3), because of $\tau_S = 18.0$ ps (Figure 4c) and T in the order of ns. Fitting by Equation (3) worked well, as indicated by the black curve in Figure 4e, and determined the τ_L to be 4.4 ± 0.5 ns. We note that decay curve off the metasurface was not successfully measured because of the extremely low-signal level.

The parameters C and D in Equation (3) are proportional to the initial populations contributing to the fast and slow exciton-PL components, respectively. It was determined from the fitting result in Figure 4e that C:D was 151.7:1, implying that the dominant populations were consumed as the fast component. This analysis suggests that there are two possible excitonic transitions in the TMDC monolayer. A theoretical study on the exciton band of MoS_2 monolayer showed that the A excitons have K–K direct and K–Γ intervalley transitions at approximately the same energy,[55] where Γ and K denote the high-symmetry points in the Brillouin zone. Because WS_2 is reasonably assumed to have exciton bands similar to those of MoS_2, we can ascribe the two excitonic transitions to the two observed PL components. The two PL components have not been frequently reported; however, two time-resolved studies showed the fast (ps) and slow (ns or longer) PL components in a WS monolayer.[54,56] We note that the fully integrated PL intensities at $T = \infty$ are given by the ratio of $C\tau_S$:$D\tau_L$ because the intensities are described using the double exponential functions (see the definition of $I(T)$, Equation (3)). The analysis of Figure 4e resulted in $C\tau_S$:$D\tau_L$ = 1:1.6. This ratio indicates that the slow component substantially contributed to the observed confocal image.

On the basis of the experimental results shown in Figure 4, the PL dynamics on and off the metasurfaces are depicted in **Figure** 5a,b, respectively. Excitation is indicated by the green arrow in Figure 4a. Subsequently, the photoexcited states are generated in the continuum and relax into the excitonic states or to nonradiative process(es). The excitonic states are mainly A excitons or trions owing to the emission wavelengths.[43,44] Figure 5 also shows that the A exciton energy is in matched with a peak energy of emittance on the metasurface, while the exciton off the metasurface is not enhanced by the emittance. The height of emittance is comparable in Figure 5. In addition, some excitonic states can also relax into the nonradiative process, due to exciton–exciton collisions that depend on the excitation density.[57] As is referred to in the Introduction, many attempts aiming at significant enhancement effect for the PL dynamics in 2dM have been conducted;[10–27] however, there were hardly studies to examine the whole PL dynamics described in Figure 5. Because the PL EF is a multiple quantity (Equation (2)), the three factors regarding excitation, excited-state transfer, and emission should be large simultaneously. This point of view has been neglected in the most of previous studies, which optimized only one or two of the three factors.

The PL dynamics off the metasurfaces are simpler than those on the metasurfaces because nonradiative processes are predominant, and nearly all the photoexcited states relax through the nonradiative process in an ultrafast manner. Such metal-induced quenching was studied in the 1970s using a damping oscillator model,[58] and it was determined that a fluorescent dipole located within 1 nm from an Au-film surface decayed nonradiatively at a rate exceeding 1×10^4 in comparison with the original decay rate.[31] Although this model does not address excitons in 2D materials, it can account for the heavy reduction of the PL off the metasurface. A very small portion of the photoexcited states relaxes into the excitonic state and results in the excitonic PL, as shown in the inset of Figure 4a.

In the theoretical Purcell factor evaluation, we determined that Purcell factors of approximately four can be observed in the experiment (Figure S4, Supporting Information) and that large Purcell factors are unlikely in this 2dM-fused system. The Purcell factor is equal to γ_m/γ_0 in Equation (2). From the resonant electric-field intensity, it was noted that the N_m/N_0 ratio is approximately ten. Therefore, the observed large EF implies that the η_m/η_0 ratio was approximately 25.8, reflecting a drastic change in the PL dynamics illustrated in Figure 5. This large ratio η_m/η_0 suggests suppression of metal-induced quenching.

2.4. Enhanced Raman Scattering

Figure 6a shows a typical Raman scattering spectra measured on and off the metasurface, which are shown as purple and orange lines, respectively. Raman signals coming from WS_2 appeared at 320.2, 349.7 (E^1_{2g} mode), and 415.0 cm^{-1} (A_{1g} mode), whereas those from MoS_2 are seen at 373.4 and 395.2 cm^{-1} (arrows). Although these are slightly shifted from the Raman peaks of the as-grown monolayer (Figure S5, Supporting Information), they are almost consistent with previous studies.[44,49] Interestingly, Raman scattering at 518 cm^{-1} from Si also became prominent. This is nontrivial because the top layer was Au and Si was located under the Au film. Nevertheless, the Si line was clearly observed. The Raman scattering signals of the TMDC layer off the metasurface were 11.2-fold decreased compared to those on the

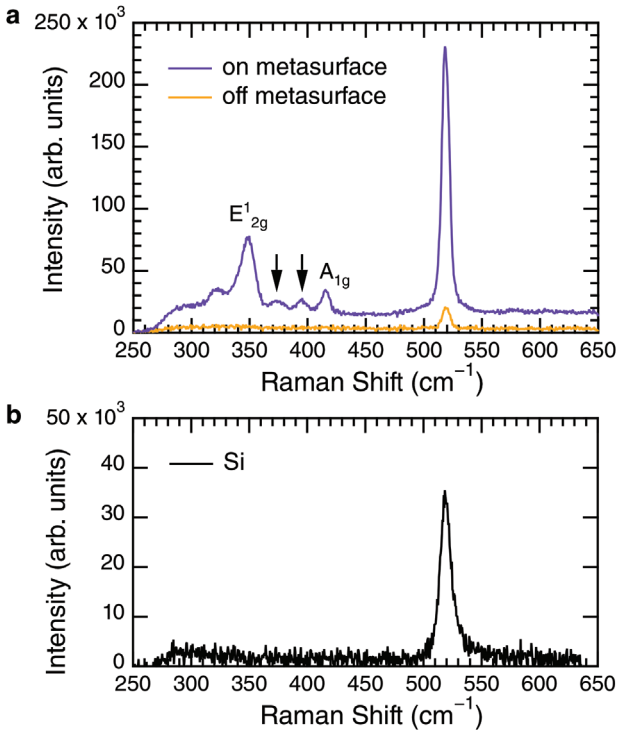

Figure 6. Enhanced Raman scattering by the metasurface. a) Enhanced Raman spectra measured on the metasurface (purple) and off the metasurface (orange), i.e., on the flat Au film. The former is much more prominent than the latter. b) Raman scattering of a Si wafer.

metasurface. The Raman signals of the TMDC layer off the metasurface were hardly detected under the same measurement conditions as those on the metasurface.

As a reference to the enhanced Raman scattering of Si, Figure 6b shows an ordinary Raman scattering spectrum of a Si wafer, displayed in a comparable scale with Figure 6a. The Raman signal of Si comprising the metasurface was 6.7-fold larger than that of the Si wafer. In the perforated structure of the metasurface, the volume of Si is reduced by 36.5%; therefore, the net increase in the Raman signals is estimated to be 10.6-fold, being one order of the signals. This magnification of the Si line is ascribed to the metasurface emittance at this wavelength, which is estimated to be approximately 50% in Figure 3b, and to the local electric fields at 532 nm (Figure 2e). When comparing the Si lines off the metasurface and those of Si wafer, the latter was 1.66-fold larger; this is reasonable because Au film of 30 nm thickness covered the Si layer off the metasurface and reduced the incident laser power in the Si layer.

3. Conclusion

We experimentally demonstrated a highly PL-enhancing compound system comprising the plasmo–photonic metasurface fused with the atomic-layer 2dM, which was nearly WS_2 monolayer. The maximum PL intensity was as large as 1033-fold at room temperature, compared with that of the 2dM on the reference flat Au film. This result evidences that this platform realizes efficient PL emissions from the 2dM with suppressing PL quenching due to the contacting Au layer. We moreover determined that the confocal image of the enhanced PL visualizes a quantum-mechanical coherent state through the analysis for photon number distribution using the Poisson distribution, and revealed that this 2dM–metasurface compound system can efficiently function as a quantum light source. The dynamics of the enhanced PL was studied by analyzing the decay time. Consequently, the two radiative components were determined to decay at 18 ps and 4.4 ns, respectively. These two components were attributed to the energy degeneracy of the *A* exciton in the TMDC monolayer. The ns component manifests itself the intervalley transition. Owing to the high emittance, which is a macroscopic property of the metasurface, the enhanced PL was primarily independent of the local nanostructures. This feature is distinct from that in the related studies focusing on local hot spots. Thanks to the high emittance, the Raman scattering of the TMDC monolayer was also found to be enhanced.

4. Experimental Section

Nanofabrication of Plasmo–Photonic Metasurfaces: Nanofabrication was performed using electron-beam lithography. The nanopatterns were drawn using a high-resolution electron-beam-drawing machine (JBX-6300FS, JEOL, Japan), and dry etching of the SOI layer was conducted using a BOSCH instrument (MUC-21 ASE-SRE Sumitomo Precision Product, Japan).

After the nanofabrication, metal deposition was conducted as follows. An adhesion Ti layer with thickness of 0.8 nm was normally deposited. Subsequently, an Au layer with thickness of 30 nm was formed via normal deposition. The stacked complementary structure of Au was confirmed in a section-view SEM image.[33] A wide-view SEM image is provided in Figure S6 (Supporting Information) to confirm structural uniformity of the metasurface.

Growth of the TMDC Atomic Layer: For the 2dM, monolayer WS_2 films were grown on *c*-plane sapphire substrates via cold-wall chemical vapor deposition at 800 °C and 50 Torr for 60 min. H_2S and $WOCl_4$ were used as sulfur and tungsten precursors, respectively. The flow rate of H_2S was 1 sccm, the feed rate of the N_2 carrier gas through the $WOCl_4$ canister was 300 sccm, and the temperature and pressure of the canister were maintained at 45 °C and 760 Torr, respectively. The total N_2 flow rate in the reactor was 2500 sccm. In addition, 0.1 sccm of O_2 was injected during the deposition of WS_2. Dragontrail glass, serving as a catalyst reservoir, was placed upstream of the sapphire substrate during growth to provide Na and K catalysts and promote the lateral growth of WS_2 with enlarged grain size. Because of the resident Mo in the growth chamber, Mo was detected in the Raman scattering (Figure S5, Supporting Information); Although the monolayer is $W_xMo_{1-x}S_2$, it was estimated that $x \geqslant 0.9$,[49] of which the most was WS_2; accordingly, the TMDC was simply refferred to as WS_2.

Transfer Process of the TMDC Atomic Layer: The as-grown monolayer WS_2 films were transferred from the sapphire substrate onto the metasurface. Before delamination, the WS_2/sapphire sample was coated with polymethyl methacrylate (PMMA) to support and protect the ultrathin WS_2. Subsequently, the PMMA/WS_2 stack was peeled off the sapphire surface by allowing deionized water to penetrate the interface between the sapphire and WS_2. Finally, the sample of PMMA/WS_2 on the metasurface was immersed in acetone at 50 °C for 60 min to remove the PMMA and cleaned in isopropanol, followed by drying with a N_2 blow. This procedure was etchant-free and conducted in a similar manner to those in previous reports.[6,45]

After the transfer, rapid temperature annealing was coducted. It started at room temperature (25 °C); the temperature was increased to 300 °C and maintained for 10 min under N_2 gas flow at 120 sccm; finally, the sample was cooled to the room temperature.

Numerical Implementations: Numerical calculations based on rigorous coupled-wave analysis[59] and scattering-matrix algorithm[60] were conducted. The two algorithms were combined and employed to evaluate the optical spectra and resonant EM field distributions of the plasmo–photonic metasurfaces.[51] The permittivities of Au and Si were taken from literature,[61,62] and those of air and SiO_2 were set to the representative values of 1.00054 and 2.1316, respectively.

PL and Raman-Scattering Measurement: The PL of WS_2 on the metasurfaces were measured using a micro-PL setup for spectrum acquisition and a confocal microscopy for spectrally resolved PL images. In the micro-PL setup, a single-mode continuous-wave laser light at a wavelength of 532.0 nm was focused on the WS_2 monolayer on the metasurface using a 50× objective lens with numerical aperture (NA) of 0.55 (M Plan Apo, Mitsutoyo, Japan) and a working distance of 13.0 mm. The laser power was set to 0.5 mW at the entrance of the objective lens. The PL from the WS_2 film was collected using the objective lens, passed through a monochromator (ISO-160, Teledyne Princeton Instruments, Trenton, NJ, USA) and acquired using a cooling charge-coupled device camera (ProEM1024HS, Teledyne Princeton Instruments).

The Raman scattering was measured using the same setup as that used for the PL measurements. The input laser power was set to 15 mW. The incident laser light was filtered using line-sharped filters passing wavelengths of 532 ± 2 nm. The scattered light was filtered using a Raman filter with optical density of six for the incident light at 532 nm. In this setup, Raman shift larger than 250 cm^{-1} was observed, as shown in Figure 6.

For the confocal PL imaging, a laser-scanning upright confocal microscope (Stellaris 5, Leica Microsystems, Wetzlar, Germany) was employed. A 5× objective lens of NA of 0.15 was used to acquire the wide confocal PL image in Figure 4b. The wavelength of excitation laser pulses of ps width and several tens of MHz repetition was set to 514.0 nm. Then, the lateral resolution was 1.748 μm. The confocal images were acquired using a photon-counting detector, which recorded photon numbers in a point-to-point manner; in total, the confocal images were formed by scanning the laser spot. By changing the gate time of the detector, the temporal growth of the PL was measured in the ns range of 0.5–11 ns, as shown in Figure 4e.

For the ps range, the PL decay time measurements were conducted using a pulsed ps laser (MIRA-OPO-X ps, Coherent, Santa Clara, CA, USA) with 76-MHz repetition, an emission wavelength of 540 nm, and the pulse width of 2 ps in the laser system. The pulsed laser light was focused using a 50 × objective lens of NA of 0.8 and a working distance of 1.0 mm (MPFLN50X, Olympys, Tokyo, Japan). The PL was collected using the same objective lens. The PL in ps ranges was acquired using a synchronously scanning streak camera (C5680, Hamamatsu Photonics, Hamamatsu, Japan) attached to a monochromator (250is, Chromex, Albuquerque, NM, USA).

Theoretical Evaluation of the Purcell Effect: When evaluating the Purcell factors shown in Figure S4 (Supporting Information), the excitons in the WS_2 layer were approximated as two-level energy quantum systems. Their Purcell factors were calculated using the macroscopic quantum electrodynamic theory. The excitation created by the electric dipole source was related to the quantum mechanical terms with the relaxation of the exciton. In real terms, the relaxation of the exciton was obtained by solving the Maxwell equations for a point dipole excitation in a complicated environment, which included the EM response of the different materials. A commercial finite-difference time-domain software (Ansys, Canonsburg, PA, USA) was used to solve the Maxwell equations. The optical responses of the different materials were determined from their experimentally measured dielectric permittivity.[62]

Physically, the Purcell factor value, $\Gamma(r, \omega)$, represents the enhancement or inhibition of the relaxation rate of the exciton when the WS_2 monolayer is placed in a nanostructured environment and compared with the reference relaxation value of the WS_2 monolayer. A reference value was evaluated for the case where the WS_2 layer was placed in a homogeneous media. In the reference media, the WS_2 excitons follow an exponential relaxation $\exp(-t/\tau_{ref})$ from the excited state to the ground state, where τ_{ref} is the reference lifetime. The presence of the nanostructured environment accelerates the relaxation by the Purcell factor value to $\exp(-\Gamma t/\tau_{ref})$. The Purcell factor is given by $\Gamma = \tau_{ref}/\tau_{NS}$, where τ_{NS} is the lifetime of the exciton in the nanostructured environment.

Supporting Information

Supporting Information is available from the Wiley Online Library or from the author.

Acknowledgements

M.I. acknowledges a partial support by JSPS KAKENHI Grant number JP20K21134 and the support system for curiosity-driven research in NIMS. T.K. thanks a support of Innovative Science and Technology Initiative for Security, Grant Number JPJ004596, ATLA, Japan. Nanofabrication was conducted in part at the Namiki Foundry and Nanofabrication Platform in NIMS. Numerical implementations for the optical spectra and EM fields were conducted using supercomputing resources at Cybersceience Center, Tohoku University.

Conflict of Interest

The authors declare no conflict of interest.

Data Availability Statement

The data that support the findings of this study are available from the corresponding author upon reasonable request.

Keywords

2D materials, luminescence enhancement, metasurface, plasmon–photon hybrid, Raman-scattering enhancement, transition metal dichalcogenide, tungsten disulfide

Received: December 26, 2023
Revised: February 25, 2024
Published online: April 3, 2024

[1] A. Splendiani, L. Sun, Y. Zhang, T. Li, J. Kim, C.-Y. Chim, G. Galli, F. Wang, *Nano Lett.* **2010**, *10*, 1271.
[2] K. F. Mak, C. Lee, J. Hone, J. Shan, T. F. Heinz, *Phys. Rev. Lett.* **2010**, *105*, 136805.
[3] B. Munkhbat, P. Wróbel, T. J. Antosiewicz, T. O. Shegai, *ACS Photonics* **2022**, *9*, 2398.
[4] M.-Y. Li, Y. Shi, C.-C. Cheng, L.-S. Lu, Y.-C. Lin, H.-L. Tang, M.-L. Tsai, C.-W. Chu, K.-H. Wei, J.-H. He, W.-H. Chang, K. Suenaga, L.-J. Li, *Science* **2015**, *349*, 524.
[5] R. Sharma, P. Sharma, K. R. Sahoo, S. Sankar, V. Awana, M. Kumar, T. N. Narayanan, *Mater. Today* **2021**, *50*, 69.
[6] P. Yang, X. Zou, Z. Zhang, M. Hong, J. Shi, S. Chen, J. Shu, L. Zhao, S. Jiang, X. Zhou, Y. Huan, C. Xie, P. Gao, Q. Chen, Q. Zhang, Z. Liu, Y. Zhang, *Nat. Commun.* **2018**, *9*, 979.
[7] X. Yang, S. Li, Y. Sakuma, *Small Methods* **2022**, *6*, 202201079.
[8] C.-C. Huang, H. Wang, Y. Cao, E. Weatherby, F. Richheimer, S. Wood, S. Jiang, D. Wei, Y. Dong, X. Lu, P. Wang, T. Polcar, D. W. Hewak, *ACS Appl. Mater. Interf.* **2022**, *14*, 42365.
[9] X. Yang, S. Li, N. Ikeda, A. Ohtake, Y. Sakuma, *Appl. Surf. Sci.* **2023**, *636*, 157756.

[10] J. Huang, G. M. Akselrod, T. Ming, J. Kong, M. H. Mikkelsen, *ACS Photonics* **2018**, *5*, 552.
[11] S. Butun, S. Tongay, K. Aydin, *Nano Lett.* **2015**, *15*, 2700.
[12] G. M. Akselrod, T. Ming, C. Argyropoulos, T. B. Hoang, Y. Lin, X. Ling, D. R. Smith, J. Kong, M. H. Mikkelsen, *Nano Lett.* **2015**, *15*, 3578.
[13] J. Kern, A. Trügler, I. Niehues, J. Ewering, R. Schmidt, R. Schneider, S. Najmaei, A. George, J. Zhang, J. Lou, U. Hohenester, S. Michaelis de Vasconcellos, R. Bratschitsch, *ACS Photonics* **2015**, *2*, 1260.
[14] S. Wang, S. Li, T. Chervy, A. Shalabney, S. Azzini, E. Orgiu, J. A. Hutchison, C. Genet, P. Samorì, T. W. Ebbesen, *Nano Lett.* **2016**, *16*, 4368.
[15] Z. Wang, Z. Dong, Y. Gu, Y.-H. Chang, L. Zhang, L.-J. Li, W. Zhao, G. Eda, W. Zhang, G. Grinblat, S. A. Maier, J. K. W. Yang, C.-W. Qiu, A. T. S. Wee, *Nat. Commun.* **2016**, *7*, 11283.
[16] H. Chen, S. Nanz, A. Abass, J. Yan, T. Gao, D.-Y. Choi, Y. S. Kivshar, C. Rockstuhl, D. N. Neshev, *ACS Photonics* **2017**, *4*, 3031.
[17] A. F. Cihan, A. G. Curto, S. Raza, P. G. Kik, M. L. Brongersma, *Nat. Photonics* **2018**, *12*, 284.
[18] J. Huang, G. M. Akselrod, T. Ming, J. Kong, M. H. Mikkelsen, *ACS Photonics* **2018**, *5*, 552.
[19] T. Bucher, A. Vaskin, R. Mupparapu, F. J. F. Löchner, A. George, K. E. Chong, S. Fasold, C. Neumann, D.-Y. Choi, F. Eilenberger, F. Setzpfandt, Y. S. Kivshar, T. Pertsch, A. Turchanin, I. Staude, *ACS Photonics* **2019**, *6*, 1002.
[20] J. Yan, Z. Zheng, Z. Lou, J. Li, B. Mao, B. Li, *Nanoscale Horiz.* **2020**, *5*, 1368.
[21] S. R. K. Indukuri, C. Frydendahl, J. Bar-David, N. Mazurski, U. Levy, *ACS Appl. Nano Mater.* **2020**, *3*, 10226.
[22] M. W. Yu, S. Ishii, S. Li, J. R. Ku, J. H. Yang, K. L. Su, T. Taniguchi, T. Nagao, K. P. Chen, *npj 2D Mater. Appl.* **2021**, *5*, 47.
[23] Y. Niu, H. Xu, H. Wei, *Phys. Rev. Lett.* **2022**, *128*, 167402.
[24] B. Du, Y. Li, M. Jiang, H. Zhang, L. Wu, W. Wen, Z. Liu, Z. Fang, T. Yu, *Nano Lett.* **2022**, *22*, 1649.
[25] S. I. Azzam, K. Parto, G. Moody, *Nanophotonics* **2023**, *12*, 477.
[26] M. Zhang, Y. Tian, X. Chen, Z. Sun, X. Zhu, J. Wu, *Nanophotonics* **2023**, *12*, 3267.
[27] M. Iwanaga, X. Yang, V. Karanikolas, T. Kuroda, Y. Sakuma, *Nanophotonics* **2024**, *13*, 95.
[28] S. Wu, S. Buckley, J. R. Schaibley, L. Feng, J. Yan, D. G. Mandrus, F. Hatami, W. Yao, J. Vučković, A. Majumdar, X. Xu, *Nature* **2015**, *520*, 69.
[29] M. Iwanaga, B. Choi, *Nano Lett.* **2015**, *15*, 1904.
[30] J.-J. Greffet, M. Nieto-Vesperinas, *J. Opt. Soc. Am. A* **1998**, *15*, 2735.
[31] B. Choi, M. Iwanaga, H. T. Miyazaki, Y. Sugimoto, A. Ohtake, K. Sakoda, *Chem. Commun.* **2015**, *51*, 11470.
[32] M. Iwanaga, B. Choi, H. T. Miyazaki, Y. Sugimoto, *Nanoscale* **2016**, *8*, 11099.
[33] M. Iwanaga, *Biosens. Bioelectron.* **2021**, *190*, 113423.
[34] M. Iwanaga, *Appl. Sci.* **2018**, *8*, 1328.
[35] Z. Dong, S. Gorelik, R. Paniagua-Dominguez, J. Yik, J. Ho, F. Tjiptoharsono, E. Lassalle, S. D. Rezaei, D. C. J. Neo, P. Bai, A. I. Kuznetsov, J. K. W. Yang, *Nano Lett.* **2021**, *21*, 4853.
[36] M. Iwanaga, *ACS Nano* **2020**, *14*, 17458.
[37] M. Iwanaga, *Biosensors* **2021**, *11*, 33.
[38] M. Iwanaga, W. Tangkawsakul, *Biosensors* **2022**, *12*, 981.
[39] M. Iwanaga, *Biosensors* **2022**, *12*, 987.
[40] M. Iwanaga, *Biosensors* **2023**, *13*, 377.
[41] M. Iwanaga, T. Hironaka, N. Ikeda, T. Sugasawa, K. Takekoshi, *Nano Lett.* **2023**, *23*, 5755.
[42] K. Momma, F. Izumi, *J. Appl. Crystallogr.* **2011**, *44*, 1272.
[43] T. Aihara, R. Wang, X. Yang, Y. Sakuma, A. O. Okano, M. Ikezawa, *Jpn. J. Appl. Phys.* **2022**, *61*, 071003.
[44] K. M. McCreary, A. T. Hanbicki, S. Singh, R. K. Kawakami, G. G. Jernigan, M. Ishigami, A. Ng, T. H. Brintlinger, R. M. Stroud, B. T. Jonker, *Sci. Rep.* **2016**, *6*, 35154.
[45] F. Zhang, C. Erb, L. Runkle, X. Zhang, N. Alem, *Nanotechnol.* **2018**, *29*, 025602.
[46] Y. Fu, D. He, J. He, A. Bian, L. Zhang, S. Liu, Y. Wang, H. Zhao, *Adv. Mater. Interf.* **2019**, *6*, 1901307.
[47] A. O. A. Tanoh, J. Alexander-Webber, J. Xiao, G. Delport, C. A. Williams, H. Bretscher, N. Gauriot, J. Allardice, R. Pandya, Y. Fan, Z. Li, S. Vignolini, S. D. Stranks, S. Hofmann, A. Rao, *Nano Lett.* **2019**, *19*, 6299.
[48] S. Tongay, W. Fan, J. Kang, J. Park, U. Koldemir, J. Suh, D. S. Narang, K. Liu, J. Ji, J. Li, R. Sinclair, J. Wu, *Nano Lett.* **2014**, *14*, 3185.
[49] X. An, W. Zhao, Y. Yu, W. Wang, T. Zheng, Y. Cui, X. Yuan, J. Lu, Z. Ni, *Appl. Phys. Lett.* **2022**, *120*, 172104.
[50] Z. Luo, W. Zheng, N. Luo, B. Liu, B. Zheng, X. Yang, D. Liang, J. Qu, H. Liu, Y. Chen, Y. Jiang, S. Chen, X. Zou, A. Pan, *Nano Lett.* **2022**, *22*, 2112.
[51] M. Iwanaga, *Plasmonic Resonators: Fundamentals, Advances, and Applications*, Pan Stanford Publishing, Singapore **2016**.
[52] E. M. Purcell, *Phys. Rev.* **1946**, *69*, 681.
[53] R. Loudon, *The Quantum Theory of Light*, 3rd edition, Oxford Univ. Press, Oxford, UK **2000**, ch. 5.
[54] T. Kuroda, Y. Hoshi, S. Masubuchi, M. Okada, R. Kitaura, K. Watanabe, T. Taniguchi, T. Machida, *Phys. Rev. B* **2020**, *102*, 195407.
[55] F. Wu, F. Qu, A. H. MacDonald, *Phys. Rev. B* **2015**, *91*, 075310.
[56] N. Mondal, N. Azam, Y. N. Gartstein, M. Mahjouri-Samani, A. V. Malko, *Adv. Mater.* **2022**, *34*, 2110568.
[57] Y. Hoshi, T. Kuroda, M. Okada, R. Moriya, S. Masubuchi, K. Watanabe, T. Taniguchi, R. Kitaura, T. Machida, *Phys. Rev. B* **2017**, *95*, 241403.
[58] R. R. Chance, A. Prock, R. Silbey, *Adv. Chem. Phys.* **1978**, *37*, 1.
[59] L. Li, *J. Opt. Soc. Am. A* **1997**, *14*, 2758.
[60] L. Li, *J. Opt. Soc. Am. A* **1996**, *13*, 1024.
[61] A. D. Rakić, A. B. Djurišić, J. M. Elazar, M. L. Majewski, *Appl. Opt.* **1998**, *37*, 5271.
[62] E. D. Palik, *Handbook of Optical Constants of Solids II*, Academic, San Diego, USA **1991**.